Tunable topological transitions in the frustrated magnet HoAgGe

Hari Bhandari,[1,2,3,*] Po-Hao Chang,[3,4] Resham Babu Regmi,[1,2] Bence Gábor Márkus,[1,2] László Forró,[1,2] J.F. Mitchell,[5] I. I. Mazin,[3,4] and Nirmal J. Ghimire[1,2,†]

[1] *Department of Physics and Astronomy, University of Notre Dame, Notre Dame, IN 46556, USA*
[2] *Stravropoulos Center for Complex Quantum Matter, University of Notre Dame, Notre Dame, IN 46556, USA*
[3] *Department of Physics and Astronomy, George Mason University, Fairfax, VA 22030, USA*
[4] *Quantum Science and Engineering Center, George Mason University, Fairfax, VA 22030, USA*
[5] *Materials Science Division, Argonne National Laboratory, Lemont, IL, 60439, USA*

The kagome lattice, known for its strong frustration in two dimensions, hosts a variety of exotic magnetic and electronic states. A variation of this geometry, where the triangular motifs are twisted to further reduce symmetry, has recently revealed even more complex physics. HoAgGe exemplifies such a structure, with magnetic and electronic properties believed to be driven by strong in-plane anisotropy of the Ho spins, effectively acting as a two-dimensional spin ice. In this study, using a combination of magnetization, Hall conductivity measurements, and density functional theory calculations, we demonstrate how various spin-ice states, stabilized by external magnetic fields, influence the Fermi surface topology. More interestingly, we observe sharp transitions in Hall conductivity without concurrent changes in magnetization when an external magnetic field is applied along a particular crystallographic direction, underscoring the role of strong magnetic frustration and providing a new platform for exploring the interplay between magnetic frustration, electronic topology, and crystalline symmetry. These results also highlight the limitations of a simple spin-ice model, suggesting that a more sophisticated framework is necessary to capture the subtle experimental nuances observed.

I. INTRODUCTION

Magnetic frustration is widely known to give rise to a variety of exotic phases, such as quantum spin liquids and spin ice states, which host novel particles such as Majorana fermions and magnetic monopoles [1–3]. Among highly frustrated systems, kagome magnets stand out [4]. In a kagome lattice, corner-sharing equilateral triangles form perfect hexagons. When these triangles are rotated with respect to each other, they create what is called "twisted kagome lattice" [5, 7], reducing symmetry and increasing in-plane anisotropy. Additionally, in systems involving rare earth elements, the crystal field splitting introduces an additional energy scale [9]. In scenarios where the electronic bands near the Fermi energy are derived from the rare earth, there is a unique opportunity to tune magnetism by manipulating anisotropies through external parameters such as magnetic fields. This tuning becomes even more compelling if the electronic bands exhibit topological features, such as flat bands and Dirac or Weyl points–key areas of interest in condensed matter physics.

HoAgGe features a twisted kagome net formed by a rare earth element Ho [9]. It has a non-centrosymmetric crystal structure $P\bar{6}2m$, with alternating layers of Ho_3Ge and Ag_3Ge_2 along the [001] direction (Fig. 1(a)). The equilateral triangles in the lattice are rotated by $\approx 15.6°$ around the c-axis [8], forming the twisted kagome network shown in Fig. 1(b). Previous studies have revealed that HoAgGe undergoes two successive antiferromagnetic transitions at 11 K (T_{N1}), and 7 K (T_{N2}) [8–12]. Below T_{N1}, the spins in Ho atoms partially order, while a fully ordered magnetic state emerges below T_{N2} [8].

Given the large single-site magnetic anisotropy energy (MAE) of the f-electrons, the low-temperature ground state has been interpreted as a $\sqrt{3} \times \sqrt{3}$ kagome spin ice, as shown in Fig. 1(c) [7]. There are three distinct types of Ho spins: Ho_1 with spins along [120], Ho_2 with a positive projection along [120], and Ho_3 with a negative projection along [120] as labelled in Fig. 1(c).

We refer to the ground-state phase, based on the orientation of the Ho_1 spins, as the up-down-down (UDD) phase. When an external field is applied along the [120] direction, the flipping of the two down-oriented Ho_1 spins results in the UUD, and UUU phases, as shown in Figs. 1(d) and 1(e). As the magnetic field increases further, Ho_2 spins flip, leading to the UUU(1) phase in Fig. 1(f)]. These phases were identified as the 1-in-2-out or 2-in-1-out spin ice states in Ref. [8], where each spin flip causes a magnetization jump, creating 1/3 magnetization plateaus.

Additionally, it has been shown [7] that within the first (1/3), and the second (2/3) plateaus, time-reversal-like meta-stable ice-rule states — exhibiting identical magnetization but differing in magnetotransport properties — are stabilized, presumably due to the twisting of the Ho-kagome-net. To the best of our knowledge, the magnetic phases developed under an external field along

* hbhandar@nd.edu
† nghimire@nd.edu

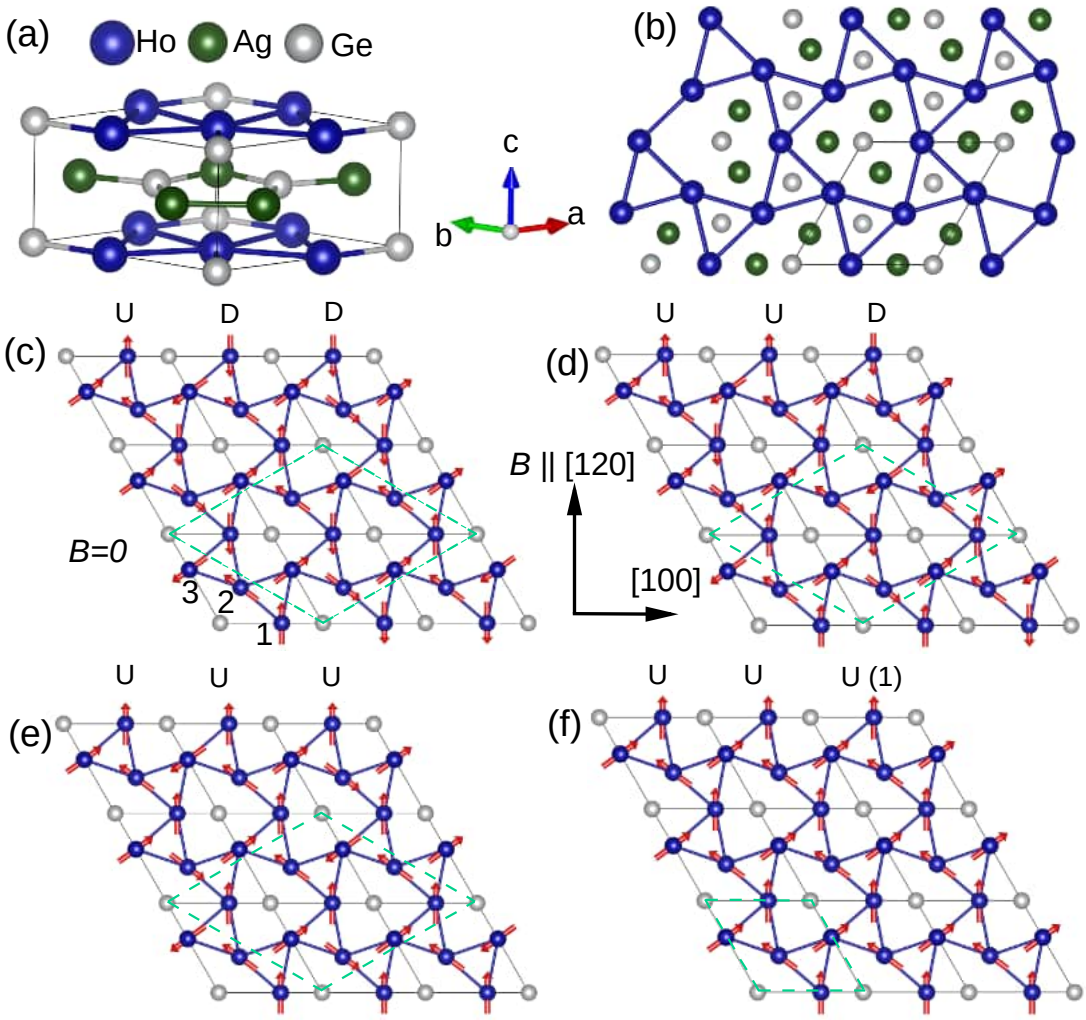

FIG. 1 : Crystal and magnetic structures of HoAgGe. a) A sketch of the crystal structure of HoAgGe. b) A view along the *c*-axis, highlighting the twisted kagome network of Ho atoms in the *ab*-plane. (c - f) The low-temperature magnetic structure of HoAgGe under different magnetic fields applied along the [120] crystallographic direction. The [120] direction, relative to the crystal plane, is indicated by the black arrow. Solid lines represent the crystallographic unit cells. Red arrows in panels c-f denote teh spin directions. "U", and "D" refer to up, and down spins, respectively. Panel (c) shows the the ground state ($B = 0$) UDD structure. The numbers 1, 2, 3 correspond to Ho_1, Ho_2, and Ho_3 atoms, as defined in the main text. At a small magnetic field B_1, one down spin (D) of Ho_1 flips, leading to the UUD structure (panel d). As the magnetic field increases to B_2, another Ho_1 down spin flips, resulting in the UUU structure (panel e). At the saturated field, B_3, spins of all Ho_3 atoms flip, producing the UUU(1) structure (panel f). These magnetic structures were determined in a previous study [8]. The green dashed lines represent the magnetic unit cell.

the [100] direction have not been previously studied, despite crystallographic differences between the two cases. Furthermore, the validity of the spin-ice model with infinite MAE has never been put to quantitative tests. There has also been no microscopic explanation proposed for the coupling of the these metastable states or for the appearance of the narrow (1/6) and (5/6) phases, identified in Ref. [8].

In this article, we investigate the impact of an in-plane magnetic field on the electronic band structure using magnetization, Hall effect measurements, and density functional theory (DFT) calculations. We find that the twisted kagome geometry leads to topologically nontrivial features such as quasi-2D bands, which have very narrow dispersion along a particular high-symmetry path in the Brillouin zone, and kagome Dirac crossings. Magnetic ordering into the ground state $\sqrt{3} \times \sqrt{3}$ supercell state results in folding of these bands, leading to a change in Fermi surface topology. External magnetic field-induced spin flipping that does not alter the supercell structure has little effect on the electronic structure, even with a substantial change in magnetization. However, when a

spin flip transforms the supercell into the 1×1 structure, a significant change in Fermi surface topology occurs, causing an abrupt reversal in the Hall conductivity sign thereby regaining the quasi-2D and Dirac bands closer to the Fermi energy and with a significant spin polarization, a much-anticipated outcome of band structure manipulation by an external magnetic field. Even more intriguing, when the external magnetic field is aligned along the crystallographic a-axis, the Hall conductivity exhibits significant changes in Fermi surface topology without a corresponding change in magnetization. This anomalous behavior is attributed to magnetic field-induced frustration caused by the distortion of the perfect kagome geometry. These findings highlight the twisted kagome lattice as an important platform for exploring the interplay between magnetism and band topology.

II. RESULTS AND DISCUSSION

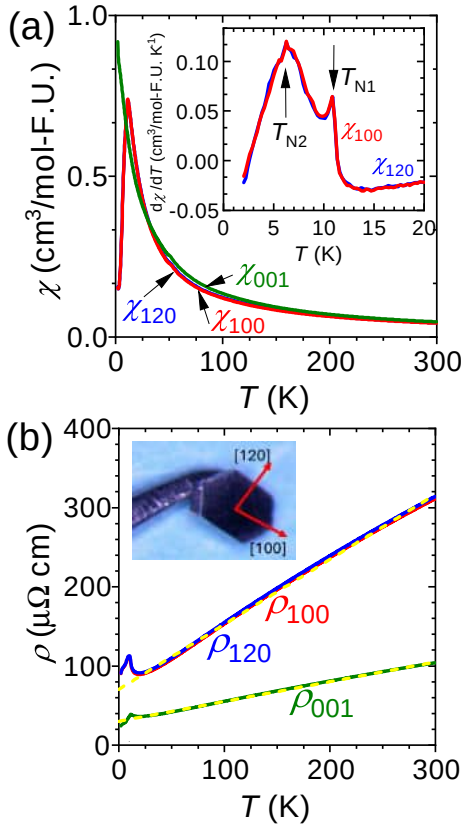

FIG. 2 : Physical properties characterization of HoAgGe. a) Magnetic susceptibility measured with an external magnetic field of 0.1 T along [100], [120], and [001] directions using the field-cooled protocol. b) Electrical resistivity as a function of temperature, $\rho(T)$, measured with current applied along [100], [120], and [001] directions. The yellow lines represent linear fits to $\rho(T)$ above 30 K. The inset shows an optical image of a polished crystal, illustrating crystallographic directions within the ab-plane.

A. Magnetic susceptibility and resistivity

The magnetic susceptibility (χ) and longitudinal resistivity (ρ) along the three crystallographic directions [100], [120] and [001] are shown in Fig. 2. A clear antiferromagnetic transition at 11 K (T_{N1}) is observed in χ_{100} and χ_{120}, while χ_{001} shows a steady increase down to 1.8 K, the lowest temperature measured [Fig. 2(a)]. Nevertheless, T_{N1} is detected in the resistivity along all three directions [Fig. 2(b)]. Furthermore, both T_{N1} and T_{N2} are evident in the derivative of susceptibility [see the inset of Fig. 2(a)] and of resistivity (Supplementary Fig. S1). This is consistent with previous studies [8–12]. The in-plane resistivities both along [100] (ρ_{100}) and [120] (ρ_{120}) are almost identical, and in the entire temperature range larger than the out-of-plane resistivity ρ_{001}, suggesting an anisotropic Fermi surface [13]. Additionally, in the non-magnetic state, resistivity in either direction above 30 K is approximately linear in temperature, shown by the yellow lines in Fig. 2(b).

B. Magnetization and Hall conductivity

In this study, we focus on comparing Hall conductivity with magnetization, particularly in the magnetic states below T_{N2}. Figure 3(a) shows the magnetization (M, in blue), and Hall conductivity (σ_{xz}, in red) for B||[120] at 1.8 K. Here σ_{xz} is measured with current I along [100] and Hall voltage along [001]. The magnetization curve exhibits three major jumps at the fields $B_1 = 0.8$ T, $B_2 = 2.1$ T, and $B_3 = 3.2$ T, corresponding to metamagnetic transitions from ground state UDD to UUD, UUU, and UUU(1) states, forming the 1/3 plateaus, as depicted in Figs. 1(c-f). Importantly, it does not fully saturate above B_3, but keeps increasing at a sizeable rate of approximately 0.15 μ_B/T, suggesting that the assumed Ising MAE is large, but not dominant.

In addition, two smaller jumps in M appear just above B_1 and B_2 corresponding to 1/6 and 5/6 magnetization plateaus, also observed previously [7, 8]. Regarding Hall conductivity, σ_{xz} shows a positive slope below B_3, with slight changes corresponding to each of the M jumps. At B_3, σ_{xz} abruptly changes sign and decreases by about 1600 S/cm before levelling off. Notably, $\sigma_{xz}(B)$ is not linear like M in the saturated [UUU(1)] state. In the UUD and UUU states, the plateaus in σ_{xz} are clearly split, while those in M are not. This hysteretic behavior in Hall conductivity has been attributed in Ref. [8] to time-reversal-like metastable toroidal spin-ice structures with opposite chirality, although the microscopic mechanism of coupling toroidicity with the magnetic field is unclear.

When the field is applied along the [100] direction, which is qualitatively different from [120] (see Fig. 3(b)), three main magnetization steps are again observed at $B_1 = 0.9$ T, $B_2 = 2.1$ T, and $B_3 = 2.6$ T. Notably, between $B = 0$ and B_2, the magnetization along [100], and

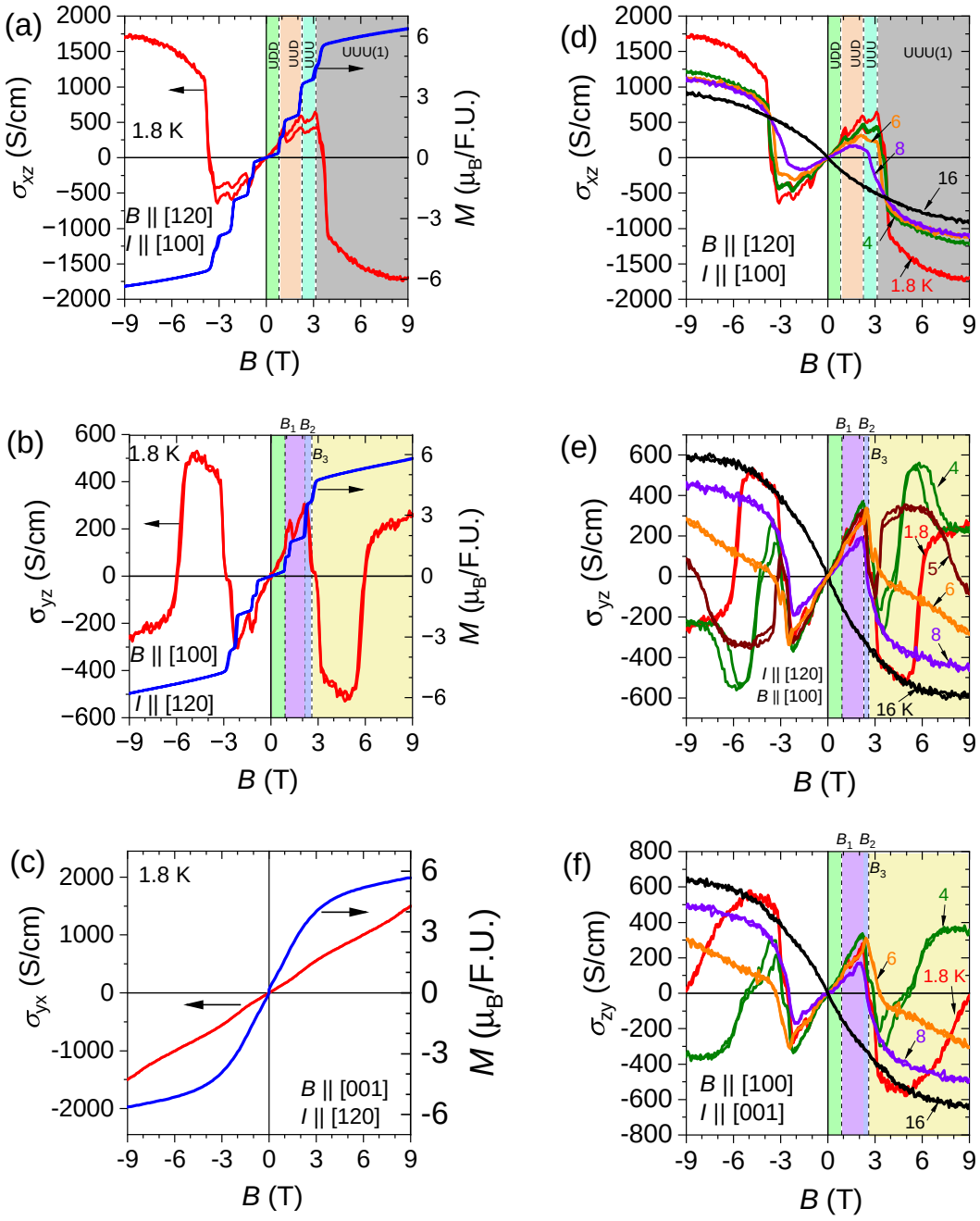

FIG. 3 : Magnetization and Hall Conductivity measured with magnetic field B and current I applied along different crystallographic directions. (a-c) Hall conductivity (red curve, plotted on the left axis) and magnetization (blue curve, plotted on the right axis) as a function of magnetic field for magnetic field B||[120] and I||[100] (a), B||[100] and I||[120] (b), and B||[001] and I||[120] (c). (d-f) Hall conductivity as a function of magnetic field at various temperatures for B||[120] and I||[100] (d), B||[100] and I||[120] (e), and B||[100] and I||[001] (f). Dashed lines and shaded regions of different colors serve as guides for the eye, indicating transitions at the magnetic fields B_1, B_2, and B_3 observed in the magnetization measurements.

[120] overlaps (see supplementary Fig. S3(a)). However, B_3||[100] is approximately 0.6 T lower than B_3||[120], and the magnetization along [100] is about 0.4 μ_B per F.U. less than that along [120], consistent with the net x and y projection ratio in the twisted kagome geometry, $2/\sqrt{3} \approx 1.15$. Meanwhile, the differential susceptibility dM/dT above B_3 is the same for both the [100] and [120] direction.

The Hall conductivity σ_{yz} presented in Fig. 3(b) shows a positive slope below B_2, similar to that of σ_{xz},

and drops sharply above B_2, resembling the behavior of σ_{xz} at B_3. While $|\sigma_{xz}|$ continues to increase steadily after the drop at B_3, $|\sigma_{yz}|$ initially increases similarly to σ_{xz} after the drop at B_2, up to about $B \approx 5$ T, at which point it rises sharply. There is no corresponding feature in magnetization for this sharp rise in σ_{xz}, highlighting a complete decoupling between Hall conductivity and net magnetization. This behavior resembles the σ_{xz} plateaus in the UUD and UUU states [7], but in this case, the change in σ_{yz} without any alteration in magnetization is far more pronounced, pointing to a new and significant magnetism effect on the electronic band structure without any effect on magnetization. To the best of our knowledge, such a drastic change in Hall conductivity without any change in the M response has not been reported in any other materials.

Finally, when B is applied along [001] direction, the magnetization (M) increases steadily, with a very large slope at small fields, $dM/dT \approx 1.6\mu_B$/T. Around 3 T the slope gradually changes, reaching a similar slope to the in-plane response only near 9 T. The implications of this behavior, which are inconsistent with the spin-ice model, are presented below in the Discussion section. The Hall conductivity σ_{yx} maintains a positive slope across the entire field range from 0 to 9 T, with only a slight slope change near 3 T as depicted in Fig. 3(c). It is worth noting that the slope magnitude of σ_{xz}, σ_{yz}, and σ_{yx} below 2 T remain fairly consistent, ranging from $\sim$ 120 to 160 S/cm-T, suggesting that carrier concentration remains nearly constant in these cases.

To get a deeper insight into the various features observed, particularly in σ_{xz} and, σ_{yz}, we analyzed their temperature dependence for different directions of I and B. Figure 3(d) illustrates the behavior of σ_{xz} as the temperature decreases from 16 K to 1.8 K. At 16 K, σ_{xz} exhibits an overall negative slope, indicating that electrons are the dominant carriers. Just below $T_{\rm N1}$, σ_{xz} exhibits a slight positive slope, suggesting that holes have become the primary charge carriers, as seen in the 8 K data (additional temperatures are provided in Supplementary Fig. S4). However, at B_3, σ_{xz} drops sharply, and returns to a negative slope, similar to the behavior observed at 16 K data. This trend in σ_{xz} continues as the temperature decreases to 1.8 K. Above B_3, the magnitude of σ_{xz} increases progressively as the temperature decreases from $T_{\rm N2}$ to 4 K. Nevertheless, a significant increase in this magnitude is observed between 4 K and 1.8 K, indicating the emergence of an additional Hall signal at 1.8 K.

The temperature dependence of σ_{yz} is depicted in Fig. 3(e). After the B_2 drop, the magnitude of σ_{yz} at 1.8 K does not exceed its value at 16 K, which corresponds to the non-magnetic state. Between B_2 and 5 T at 1.8 K, σ_{yz} tracks the 16 K data. However, above 5 T, the 1.8 K data turns sharply followed by a curving off. This upturn and subsequent curving off are observed on warming up to 5 K, but disappear at 6 K. At and above 6 K, $|\sigma_{yz}|$ shows a monotonic increase with the magnetic field after the initial drop. Notably, σ_{yz} does not display hysteresis at 1.8 K, although significant hysteresis is observed at 4 K during the initial upturn and the subsequent downturn, centered at around 3.2 and 7 T, respectively. At 5 K, the hysteresis is observed only after the first upturn. Similar Hall conductivity behavior is observed when current and voltage directions are reversed, with the magnetic field aligned along [100] (σ_{zy}) as depicted in Fig. 3(f). The behavior below B_2 remains consistent, but above B_2, the sharp slope changes in σ_{zy} shift slightly toward higher B.

In summary, Hall conductivity measurements reveal four notable features: (1) The Hall conductivity, which shows electron-like behavior in the non-magnetic state, shifts to hole-like behavior with magnetic ordering below B_2 and B_3 for magnetic fields aligned along the [100] and [120] directions, respectively. (2) At $B_2||[100]$ and $B_3||[120]$, there is an abrupt sign change in Hall conductivity, reverting to electron-like behavior. (3) A significant enhancement in Hall conductivity is observed immediately after the B_3 sign change, particularly below 4 K, when B is applied along the [120] direction. (4) Below T_{N2}, Hall conductivity below 5 K measured with B along [100] exhibits multiple changes after the B_2 drop without any corresponding change in magnetization.

C. Electronic band structure calculations

To understand the microscopic origins of these Hall conductivity features, we performed electronic band structure calculations, as depicted in Fig. 4. These calculations were conducted in three states: the non-magnetic state, the magnetic UUD state, and the UUU(1) state. As shown in Figs. 1(c-e), the UDD, UUD, and UUU states share the same $\sqrt{3} \times \sqrt{3}$ magnetic unit cell. However, in the UUU(1) state, the magnetic unit cell is reduced to 1×1, the same as in the non-magnetic state, but with ordered spins.

The band structure in the non-magnetic state, shown in Fig. 4(a), reveals a large electron pocket along the hexagonal first Brillouin zone boundary, and two smaller hole pockets located along $\Gamma - A$. The electron pockets generate the electron-like Hall conductivity, especially for in-plane measurements. Fig. 4(a) shows, $\sim$ 150 meV above the Fermi energy, these quasi-2D bands hardly changing along MK but highly dispersive along $M - \Gamma$, and $K - \Gamma$, forming a Dirac-like crossing at K.

With the onset of antiferromagnetic ordering, in the UUU state, as shown in Fig. 4(b), the band structure becomes considerably more complex due to band folding from the tripled unit cell. The individual pockets, first of all, the electron donuts in Fig. 4(d), reconnect and the topology of the Fermi surface changes dramatically — even though the band's dispersion changes only moderately. Experimental evidence of hole-like conductivity in this state suggests that the reconnection of the electron pockets makes them hole-like, which, although challenging to quantify, is reflected in the band structure. The small spikes observed in Hall conductivity at

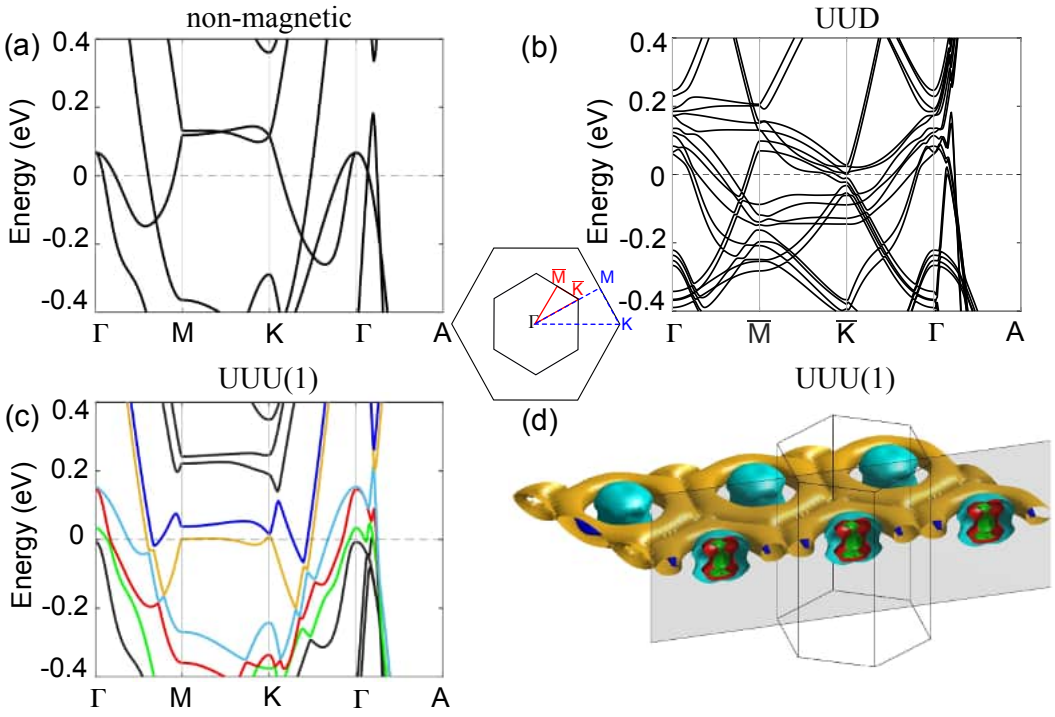

FIG. 4 : Calculated electronic structure of HoAgGe (a) Band structure in the non-magnetic state. (b) Electronic structure in $\sqrt{3} \times \sqrt{3}$ magnetic state UUD. (c) Electronic structure in 1×1 [UUU(1)] stae. (d) Fermi surface in the UUU(1) state. In the nonmagnetic state Fermi surface is very similar, with the main difference being that the orange donuts are disconnected, though they retain the electron character. The colors correspond to those in panel (c).

B_1 and B_2 correspond to spin flips at these magnetic fields. However, these spin flips do not significantly alter the magnetic unit cell, resulting in minimal changes to the sign and magnitude of the Hall conductivity. This is further supported by the overall positive slope of σ_{yx} in Fig. 3(c) where the magnetic unit cell does not change.

In the UUU(1) state, the magnetic unit cell reduces to 1×1, eliminating band folding and resulting in a Fermi surface similar to the non-magnetic state, shown in Fig. 4(c). The magnetic ordering induces spin splitting, pushing the quasi-2D bands and Dirac-like crossings to the Fermi energy, which makes the orange donuts touch but does not change their character, restoring the electron-like Hall conductivity. Consequently, above B_3, where the UUU(1) magnetic structure stabilizes, the sign of the hole conductivity changes.

A more rigorous verification of the calculated band structure, particularly the Fermi surface, comes from the longitudinal transport. We calculated the plasma frequency in the paramagnetic state and found that $\omega_{pz}^2 \approx 3.2\omega_{px}^2$. Using the basic Drude model, where $\sigma_\alpha = \omega_{p\alpha}^2\tau_\alpha/4\pi$ (with τ_α representing the anisotropic relaxation time), we observed that the resistivity shown in Fig. 2, is almost identical for the [120] and [100] directions, as expected. Additionally, above $\sim$ 30 K, it follows a perfectly linear trend, indicating that the primary scattering mechanisms are spin fluctuations with energy $\lesssim 4 \times 30k_B \sim 10$ meV. This agrees with the exchange coupling estimate from Ref. [8], and our first-principles calculations presented in detail in the Supplementary Information section S1. The resistivity in this range is well described by $\rho_x(T)$=70.6+0.82T, $\rho_z(T)$=30.1+0.25T $\mu\Omega$·cm (see Fig. 2(b)). The ratio of the slopes is 3.28, in excellent agreement with DFT, confirming the accuracy of the calculated Fermi surface. Note that the ratio of the constant terms above is smaller, 2.34, indicating that scattering off defects is anisotropic, with τ_x about 30% smaller than τ_z.

D. Discussion

The experimentally reported magnetic structures for B||[120] account for most of the observed features in the Hall conductivity σ_{xz}, including small spikes during transitions into the UUD and UUU phases, and the abrupt sign reversal in the UUU(1) phase. While these changes in the transport and magnetic properties are clearly associated with discontinuous spin reorientations, suggested in Ref. [8], several qualitative effects remain unexplained /cannot be explained by the ideal spin-ice model with infinite MAE. Thus, obtaining experimental estimates of both the exchange coupling and the MAE is crucial. To this end, we analyzed magnetization data above B_3 for

in-plane fields and over the full range for out-of-plane fields. The details are provided in the Supplementary Material section S2, where we used slopes and magnetization values in all three directions to find that the in-plane magnetic anisotropy can be described by the lowest-order term $K_{||}\cos^2\phi$ (with ϕ representing the deviation from the easy axis), and $K_{||} \approx -5.6 \pm 0.6$ meV, substantial compared to the exchange coupling but not overwhelmingly larger.

Interestingly, the out-of-plane anisotropy cannot be described as $K_\perp \cos^2\theta$ (θ characterizes tilting away from the plane). Instead, it requires higher order terms such as $K'_\perp \cos^4\theta$ and $K''_\perp \cos^6\theta$, as seen in similar studies on $R\mathrm{Mn_6Sn_6}$ compounds [9]. Moreover, the lowest-order term for out-of-plane anisotropy is anomalously soft, with $K_\perp \approx 1$ meV, suggesting very strong spin-canting fluctuations. Thus, the ideal spin-ice model is insufficient, and the unexplained features seen in this and previous studies likely arise from deviations from this model.

For $B||[100]$, the magnetic structure remains unknown. However, the Hall conductivity in this configuration suggests that, similar to $B||[120]$, a change in the magnetic unit cell leads to a sign reversal of σ_{yz}. The sign change of σ_{yz} in the UUU(1) phase, where magnetization increases linearly with B, is unexpected and intriguing. We tentatively attribute it to ordering processes in the $\mathrm{Ho_1}$ sublattice. In the limit $K \gg MB_x$ (K representing the in-plane anisotropy and M the Ho moment), the $\mathrm{Ho_1}$ spins are perpendicular to x and do not contribute to the total magnetization. In this limit, these spins do not couple either to the external field B_x or to the saturated $\mathrm{Ho_{2,3}}$ sublattices. Instead, they are coupled to each other through weak third-neighbor interaction, potentially mediated by Dzyaloshinskii-Moriya interaction (DMI) (for $\mathrm{Ho_1}$–$\mathrm{Ho_1}$ bonds, the DMI vector $\mathbf{D}||z$), which couples the x and y projections. Along with the finite stiffness of Ho spins with respect to canting away from the easy directions, this suggests that twisting the kagome lattice introduces a unique mechanism for coupling spins to the transport, driven by the resulting frustration. The irreversible Hall plateaus with the same magnetization, as observed in Ref. [8], as well as the sign-flip of the Hall conductivity without a corresponding change in magnetization seen in our work, may also stem from deviations from the ideal Ising spin dynamics.

E. Conclusion

The kagome lattice has been extensively studied for its magnetic frustration, and electronic topological properties, including flat and Dirac bands. However, the role of structural twisting in this lattice has been largely overlooked. In this regard, our findings on HoAgGe open a new pathway for investigating the interaction between structural distortion, magnetic frustration, and their influence on electronic topology. This is particularly intriguing as spin-polarized quasi-2D bands and Dirac crossings/anti-crossings are in close proximity of the Fermi energy. Additionally, HoAgGe is a part of the larger RTX family of compounds [14–19] (where R is a rare earth element, T is a transition metal, and X is either Ge or Si), providing the ability to tune magnetism through different combinations of R, T, and X atoms.

III. METHODS

Crystal growth and structural characterization. Single crystals of HoAgGe were grown by the flux method considering eucetic point of Ag-Ge. Ho pieces (Thermo Scientific 99.9%), Ag shots (Thermo Scientific 99.999%), and Ge pieces (Thermo Scientific 99.9999%) were loaded into a 2 ml aluminum oxide crucible in a molar ratio of 1:7.6:2.5. The crucible was then sealed in a fused silica ampule under vacuum. The sealed ampule was heated to 1175 °C over 10 hours, kept at 1175 °C for 10 hours, and then cooled to 825 °C over one week. Once the furnace reached 825 °C, the tube was centrifuged to separate the crystals in the crucible from the molten flux. Several well-faceted long crystals [see the inset in Fig. 2(b) for an optical image of a polished crystal] up to 150 mg were obtained in the crucible. The crystal structure was verified by Rietveld refinement [20] of a powder X-ray diffraction pattern collected on a pulverized single crystal using a Rigaku Miniflex diffractometer. The Rietveld refinement was performed using the FULLPROF software [21] and is depicted in Supplementary Fig. S7. Crystal and magnetic structures were drawn using VESTA software [22].

Physical property measurements. DC magnetization, resistivity, and Hall measurements were performed in a 9 T Quantum Design Dynacool Physical Property Measurement System (PPMS). The AC Measurement System (ACMS II) option was used for the DC magnetization measurements. Single crystals of HoAgGe were trimmed to adequate dimensions for electrical transport measurements. Crystals were oriented with the [001], [100], and [120] directions parallel to the applied field for the c-axis and ab-plane measurements. Resistivity and Hall measurements were performed using the 4-probe method. Pt wires of 25 μm were used for electrical contacts with contact resistances $< 30\ \Omega$. Contacts were affixed with Epotek H20E silver epoxy. An electric current of 4 mA was used for the electrical transport measurements. Contact misalignment in the magnetoresistance and Hall resistivity measurements were corrected, respectively, by symmetrizing and anti-symmetrizing the measured data in positive and negative magnetic fields. The magnetic and magnetotransport data presented here were measured on several samples from different growth batches to check the reproducibility.

Electronic structure calculations. Electronic structure calculations were performed using Vienna ab initio Simulation Package (VASP) [23] within projector augmented wave (PAW) method [24]. The Perdew-

Burke-Enzerhof (PBE) [25] generalized gradient approximation was employed to describe exchange-correlation effects. For the ordered states, we added a Hubbard U correction with the fully localized limit double-counting recipe [26, 27], to account for the strongly correlated Ho $4f$ states and their localized magnetic moments. The effective parameter $U - J = 8$ eV was used. The orbital moment on the Ho site obtained from the calculations is consistently 6 μ_B which satisfies Hund's rule as expected. For the paramagnetic state, the open-core approximation is employed, where the $4f$ electrons in the Ho pseudopotential are treated as part of the frozen core, simulating the average effect of the disordered magnetic moments. The plasma frequencies are obtained by integration of the Fermi velocity implemented in VASP via the LOPTICS tag [28].

ACKNOWLEDGMENTS

This work was primarily supported by the U.S. Department of Energy, Office of Science, Basic Energy Sciences, Materials Science and Engineering Division. H.B. was supported by the NSF CAREER award DMR-2143903. R.B.R was supported by Army Research Office under Cooperative Agreement Number W911NF-22-2-0173. IM was supported by the Office of Naval Research through grant #N00014-23-1-2480.

IV. REFERENCES

[1] L. Balents, Spin liquids in frustrated magnets, Nature **464**, 199 (2010).
[2] C. Castelnovo, R. Moessner, and S. L. Sondhi, Magnetic monopoles in spin ice, Nature **451**, 42 (2008).
[3] Y. Motome and J. Nasu, Hunting Majorana fermions in Kitaev magnets, Journal of the Physical Society of Japan **89**, 012002 (2020).
[4] N. J. Ghimire and I. I. Mazin, Topology and correlations on the kagome lattice, Nature materials **19**, 137 (2020).
[5] Y. N. Huang, H. O. Jeschke, and I. I. Mazin, CrRhAs: a member of a large family of metallic kagome antiferromagnets, npj Quantum Materials **8**, 32 (2023).
[7] K. Zhao, Y. Tokiwa, H. Chen, and P. Gegenwart, Discrete degeneracies distinguished by the anomalous hall effect in a metallic kagome ice compound, Nature Physics **20**, 442 (2024).
[9] Y. Lee, R. Skomski, X. Wang, P. P. Orth, Y. Ren, B. Kang, A. K. Pathak, A. Kutepov, B. N. Harmon, R. J. McQueeney, I. I. Mazin, and L. Ke, Interplay between magnetism and band topology in the kagome magnets RMn_6Sn_6, Physical Review B **108**, 045132 (2023).
[8] K. Zhao, H. Deng, H. Chen, K. A. Ross, V. Petříček, G. Günther, M. Russina, V. Hutanu, and P. Gegenwart, Realization of the kagome spin ice state in a frustrated intermetallic compound, Science **367**, 1218 (2020).
[9] E. Morosan, *Field-induced magnetic phase transitions and correlated electronic states in the hexagonal RAgGe and RPtIn series*, Ph.D. thesis (2005).
[10] S. Roychowdhury, K. Samanta, S. Singh, W. Schnelle, Y. Zhang, J. Noky, M. G. Vergniory, C. Shekhar, and C. Felser, Enhancement of the anomalous hall effect by distorting the kagome lattice in an antiferromagnetic material, Proceedings of the National Academy of Sciences **121**, e2401970121 (2024).
[11] N. Li, Q. Huang, X. Yue, S. Guang, K. Xia, Y. Wang, Q. Li, X. Zhao, H. Zhou, and X. Sun, Low-temperature transport properties of the intermetallic compound HoAgGe with a kagome spin-ice state, Physical Review B **106**, 014416 (2022).
[12] H. Deng, T. Yang, G. Liu, L. Liu, L. Zhao, W. Wang, T. Li, W. Song, T. Neupert, X.-R. Liu, *et al.*, Local Excitation of Kagome Spin Ice Magnetism Seen by Scanning Tunneling Microscopy, Physical Review Letters **133**, 046503 (2024).
[13] H. Bhandari, R. Dally, P. Siegfried, R. B. Regmi, K. Rule, S. Chi, J. Lynn, I. Mazin, and N. Ghimire, Magnetism and fermiology of kagome magnet $YMn_6Sn_4Ge_2$ (2023), npj Quantum Materials **9**, 6 (2024).
[14] F. Merlo, M. Pani, and M. Fornasini, RMX compounds formed by alkaline earths, europium and ytterbium IV: ternary phases with M = Ag and X = Si, Ge, Sn, Pb, Journal of alloys and compounds **232**, 289 (1996).
[15] A. Iandelli, The structure of ternary compounds of the rare earths: RAgSi, Journal of the Less Common Metals **113**, 25 (1985).
[16] E. Morosan, S. L. Bud'ko, and P. Canfield, Angular-dependent planar metamagnetism in the hexagonal compounds TbPtIn and TmAgGe, Physical Review B—Condensed Matter and Materials Physics **71**, 014445 (2005).
[17] S. Baran, M. Hofmann, J. Leciejewicz, B. Penc, M. Ślaski, A. Szytuła, and A. Zygmunt, Magnetic properties and magnetic structures of RAgSi (R= Gd–Er) compounds, Journal of magnetism and magnetic materials **222**, 277 (2000).
[18] Ł. Gondek and A. Szytuła, Magnetic ordering in ZrNiAl-type crystal system, Journal of alloys and compounds **442**, 111 (2007).
[19] K. Katoh, Y. Mano, K. Nakano, G. Terui, Y. Niide, and A. Ochiai, Magnetic properties of YbTGe (T= Rh, Cu, Ag), Journal of magnetism and magnetic materials **268**, 212 (2004).
[20] L. B. McCusker, R. B. Von Dreele, D. E. Cox, D. Louër, and P. Scardi, Rietveld refinement guidelines, J. Appl. Cryst. **32**, 36 (1999).
[21] J. Rodriguez-Carvajal, Recent advances in magnetic structure determination by neutron powder diffraction, Physica B **192**, 55 (1993).
[22] K. Momma and F. Izumi, Vesta 3 for three-dimensional visualization of crystal, volumetric and morphology data, Journal of applied crystallography **44**, 1272 (2011).
[23] G. Kresse and J. Furthmüller, Efficient iterative schemes for ab initio total-energy calculations using a plane-wave basis set, Physical Review B **54**, 11169 (1996).

[24] P. E. Blöchl, Projector augmented-wave method, Physical Review B **50**, 17953 (1994).

[25] J. P. Perdew, K. Burke, and M. Ernzerhof, Generalized Gradient Approximation Made Simple, Physical Review Letters **77**, 3865 (1996).

[26] A. I. Liechtenstein, V. I. Anisimov, and J. Zaanen, Density-functional theory and strong interactions: Orbital ordering in Mott-Hubbard insulators, Physical Review B **52**, R5467 (1995).

[27] S. L. Dudarev, G. A. Botton, S. Y. Savrasov, C. J. Humphreys, and A. P. Sutton, Electron-energy-loss spectra and the structural stability of nickel oxide: An LSDA+U study, Physical Review B **57**, 1505 (1998).

[28] M. Gajdoš, K. Hummer, G. Kresse, J. Furthmüller, and F. Bechstedt, Linear optical properties in the projector-augmented wave methodology, Physical Review B **73**, 045112 (2006).

Supplementary Information

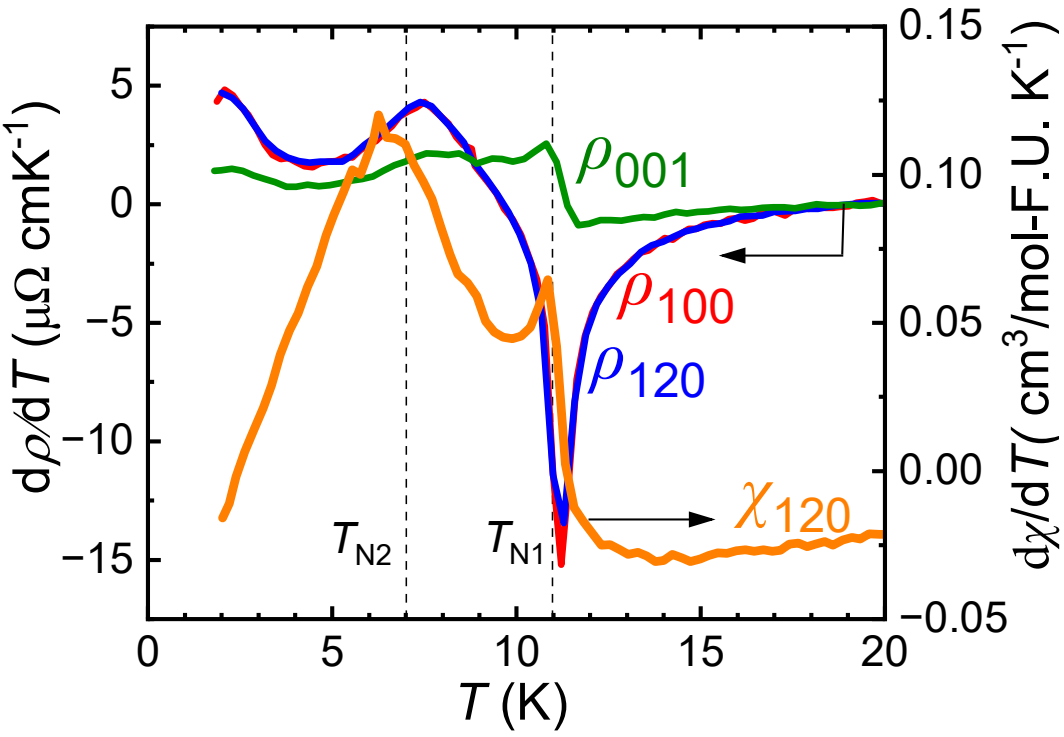

FIG. S1 : Temperature derivative of Resistivity and Susceptibility. Derivative of resistivity plotted as a function of temperature for current, I, applied along [100], [120] and [001] direction (left axis). Derivative of susceptibility for χ_{120} as a function of temperature (right axis). T_{N1} and T_{N2} represent the two Néel temperatures. The dashed lines are a guide to the eye.

S1. EXCHANGE COUPLING CONSTANTS

A numerical-orbital-based [1] DFT code OpenMX [2] was used for the calculations of magnetic properties. The exchange coupling constants up to 5th nearest neighbors (defined in Fig. S2) are calculated perturbatively using Green's function method [3, 4] implemented in OpenMX 3.9 [5, 6]. The effective spin-Hamiltonian is defined as

$$H = \sum_{\langle ij\rangle_1} J_1 \hat{n}_i \hat{n}_j + \sum_{\langle ij\rangle_2} J_2 \hat{n}_i \hat{n}_j + \sum_{\langle ij\rangle_{3a}} J_{3a} \hat{n}_i \hat{n}_j + \sum_{\langle ij\rangle_{3b}} J_{3b} \hat{n}_i \hat{n}_j + \sum_{\langle ij\rangle_4} J_4 \hat{n}_i \hat{n}_j + \sum_{\langle ij\rangle_5} J_5 \hat{n}_i \hat{n}_j, \tag{S1}$$

where $\hat{n}$ is the unit vector along local easy-axis, J_n is the exchange coupling parameters for the n-th NN interaction summarized in Table IV, and summation is over all bonds of a given type. Note that there are two inequivalent 3rd NN interactions denoted as J_{3a} and J_{3b}.

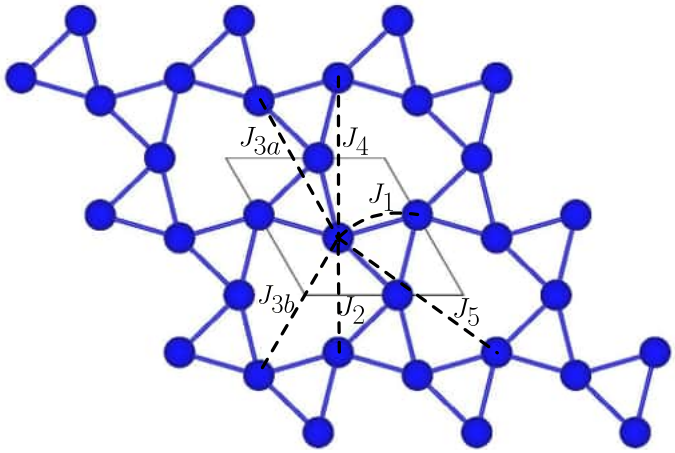

FIG. S2 : Definitions of effective exchange coupling constants up to 5 nearest neighbor.

	# of NN	meV
J_1	4	3.154
J_2	2	-1.395
J_{3a}	4	-0.412
J_{3b}	2	-0.552
J_4	2	-0.073
J_5	4	-0.212

TABLE S1 : Effective exchange coupling constants up to 5th nearest neighbor calculated using Green's function method.

S2. MAGNETIZATION

Magnetization, M, for the case of $B||[120]$ is both rich and intriguing. To fully understand the interactions within the system, it is necessary to consider all three spatial directions. Previous studies [7, 8] explained these phenomena using a "spin-ice" model, which assumes infinite easy-axis anisotropy, with the axis orientation varying from site to site according to the three-fold symmetry. However, the non-zero slope of $M(B)$ in the fully saturated spin-ice phase suggests that even at magnetic fields of about 5 T, the Ho spins are still slightly canted. This is consistent with the nonlinear Hall conductivity observed for a linear increase in magnetization (see Figs. 3(a) and S3(a)). Using this information and assuming a lowest-order in-plane angular anisotropy, we can express the total anisotropy energy for an individual site as $K_{||}M^2\cos^2(\phi-\alpha)$, where $\phi-\alpha$ is the canting angle away from the easy axis, which is assumed to be at an angle α to the Cartesian x ([100]). Zeeman energy will then be $-hM$; here M is the full moment of an individual Ho ion, and h the applied field. Note that for Ho_1 $\alpha = 90°$, and for $Ho_{2,3}$ $\alpha = \pm 30°$. Neglecting the smaller exchange coupling, we find: $\chi_{120} = [\chi_{120}(Ho_2)+\chi_{120}(Ho_3)]/3 = 1/4$K and the net magnetic moment per site: $M_{120}(B) = (2/3)M + h/4K$. Extracting these parameters from the experimental data in the saturated phase, we find $M \approx 7.7\ \mu_B$, in excellent agreement with neutron data [7], and $KM^2 \approx 6.2$ meV, a typical value for 4f ions.

Similarly, for $B||[100]$, $M_{100}(B)=(1/\sqrt{3})M + h/4K$. Here, all three ions contribute to χ. By fitting our data, we find $M \approx 7.5\ \mu_B$, $KM^2 \approx 5.0$ meV, confirming the consistency of the model (within ± 10%). This analysis shows that while the spin-ice (infinite anisotropy) model is a useful first approximation, it remains a rough one.

On the other hand, the experimentally measured $M_{001}(B)$ does not align with the spin-ice model at all. In this case, assuming a $\cos^2\phi$ easy-plane anisotropy, $\chi = 1/2K$. The low-field slope of the experimental data is at least ten times higher than the saturation-regime in-plane slope, suggesting that the quadratic anisotropy coefficient $K_2M^2 \approx 1.0$ meV. Moreover, the slope gradually decreases with increasing field, dropping to about 0.13, even lower than the in-plane values. The ramification is that the out-of-plane anisotropy is strongly non-quadratic. In f-electron ions, three terms ($\cos^2\phi$, $\cos^4\phi$, and $\cos^6\phi$) are permitted, without any parametric smallness[9]. Indeed, the nonlinear susceptibility is reasonably well described by the 6-th order Hamiltonian, $E = K_2M^2\cos^2\phi + K_4M^4\cos^4\phi + K_6M^6\cos^6\phi$, where K_2M^2 is as above, $K_4/K_2 = -0.4$, and $K_6/K_2 = 0.11$. This indicates that the out-of-plane spin dynamics differ significantly from the in-plane dynamics and are far from the strong anisotropy limit of the spin-ice

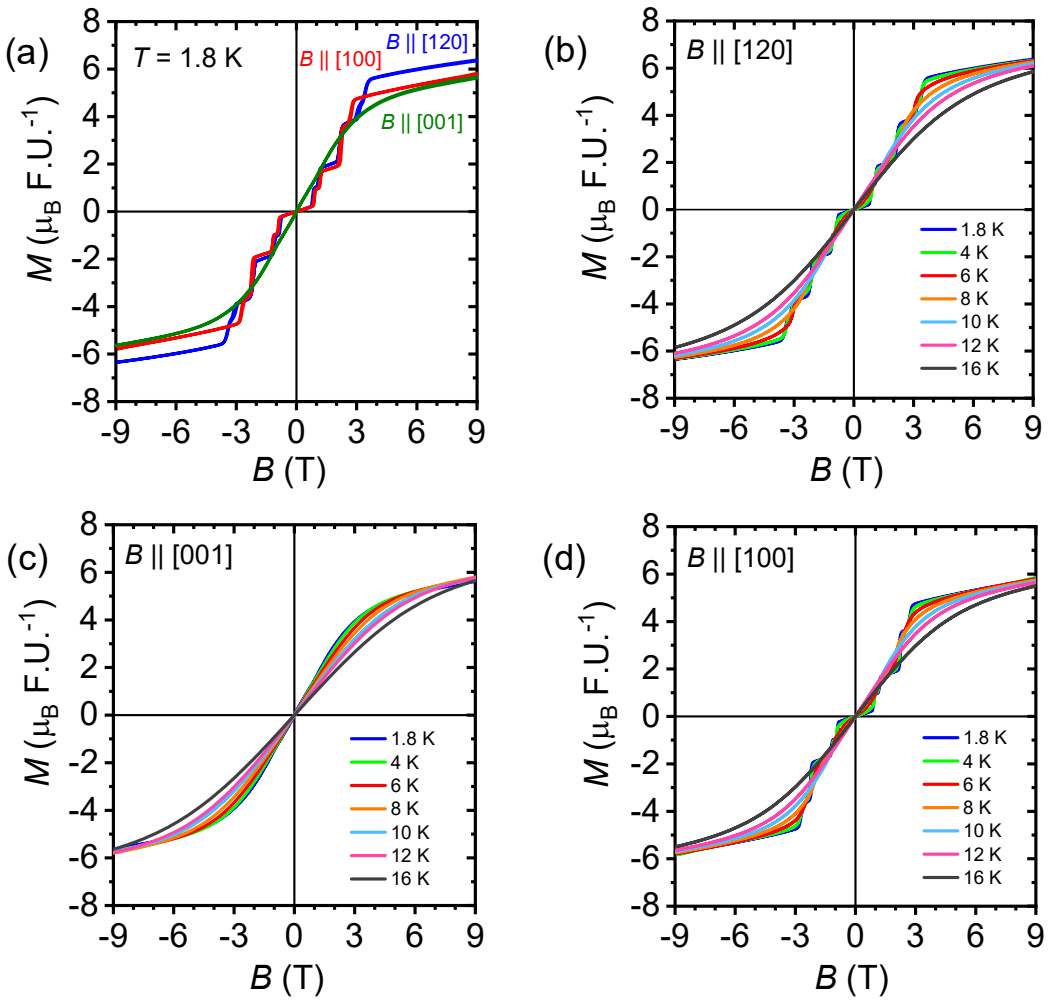

FIG. S3 : Magnetization. a) Magnetization, M, as a function of magnetic field, B at 1.8 K plotted together for B applied along the three crystallographic directions [100] (red) and [120] (blue), and [001] (green). b-d) M vs B between 1.8 and 16 K for B||[120] (b), [001] (c), and [100](d).

model. Notably, if the quartic coefficient were 60% larger, the system would transition abruptly to an easy-cone anisotropy with the cone angle approximately 30° from the plane. This effect could occur if Ho were substituted by another rare-earth element, as seen in the 166 family of materials[9].

S3. HALL CONDUCTIVITY, HALL RESISTIVITY AND MAGNETORESISTANCE

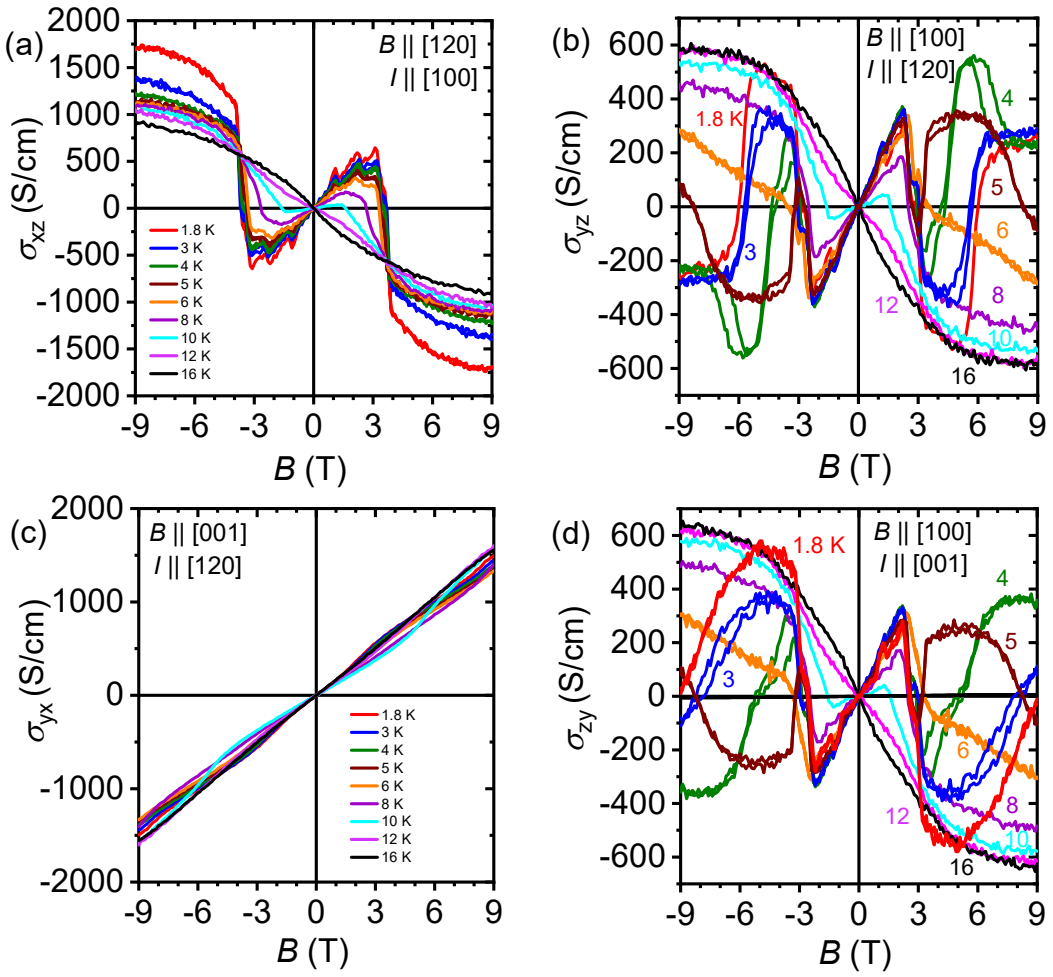

FIG. S4 : Hall conductivity. Hall Conductivity σ_{xz}, σ_{yz}, σ_{yx}, and σ_{zy} as a function of magnetic field for (a) B||[120] and I||[100] and (b) B||[100] and I||[120] (c) B||[001] and I||[120], and (d) B||[100] and I||[001], respectively.

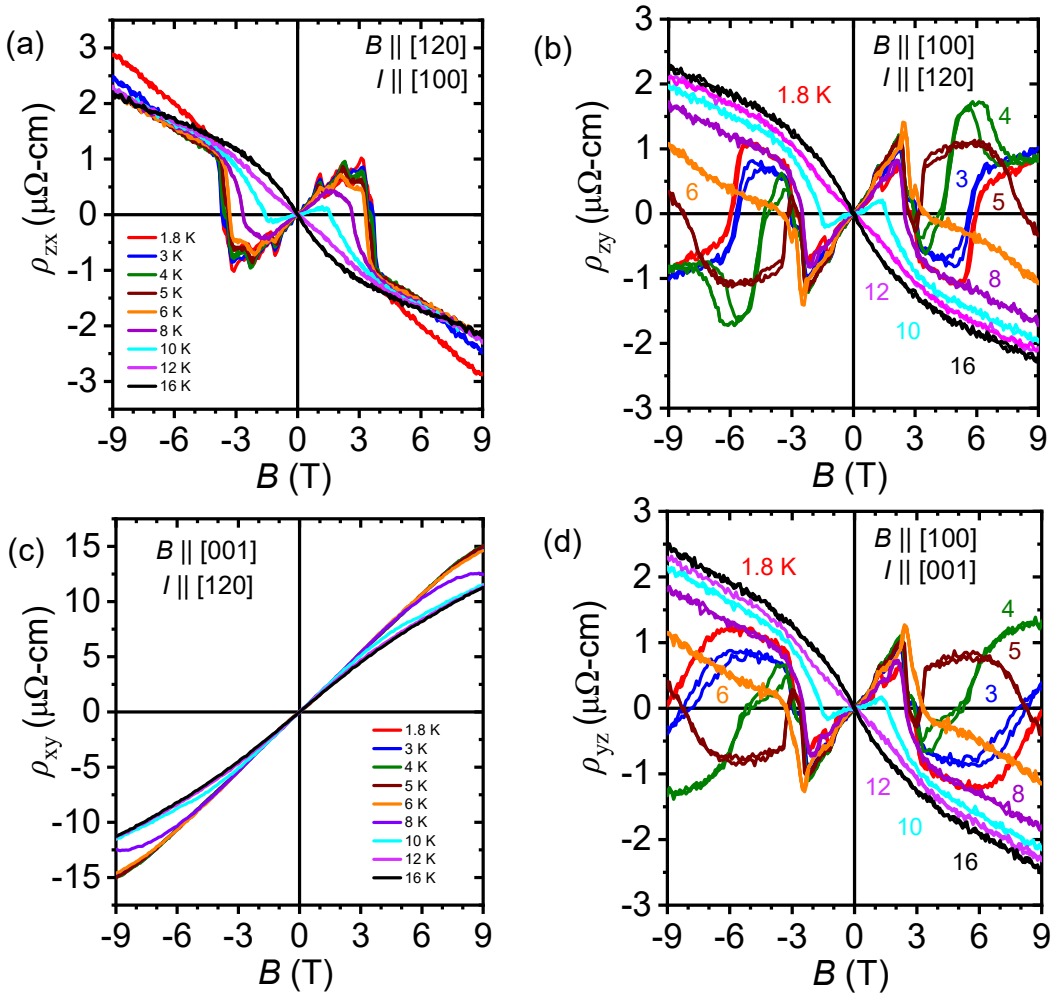

FIG. S5 : Hall resistivity. Hall resistivity ρ_{zx}, ρ_{zy}, ρ_{xy} and ρ_{yz} as a function of magnetic field (a) B|||[120] and I|||[100] and (b) B|||[100] and I|||[120] (c) B|||[001] and I|||[120], and (d) B|||[100] and I|||[001], respectively.

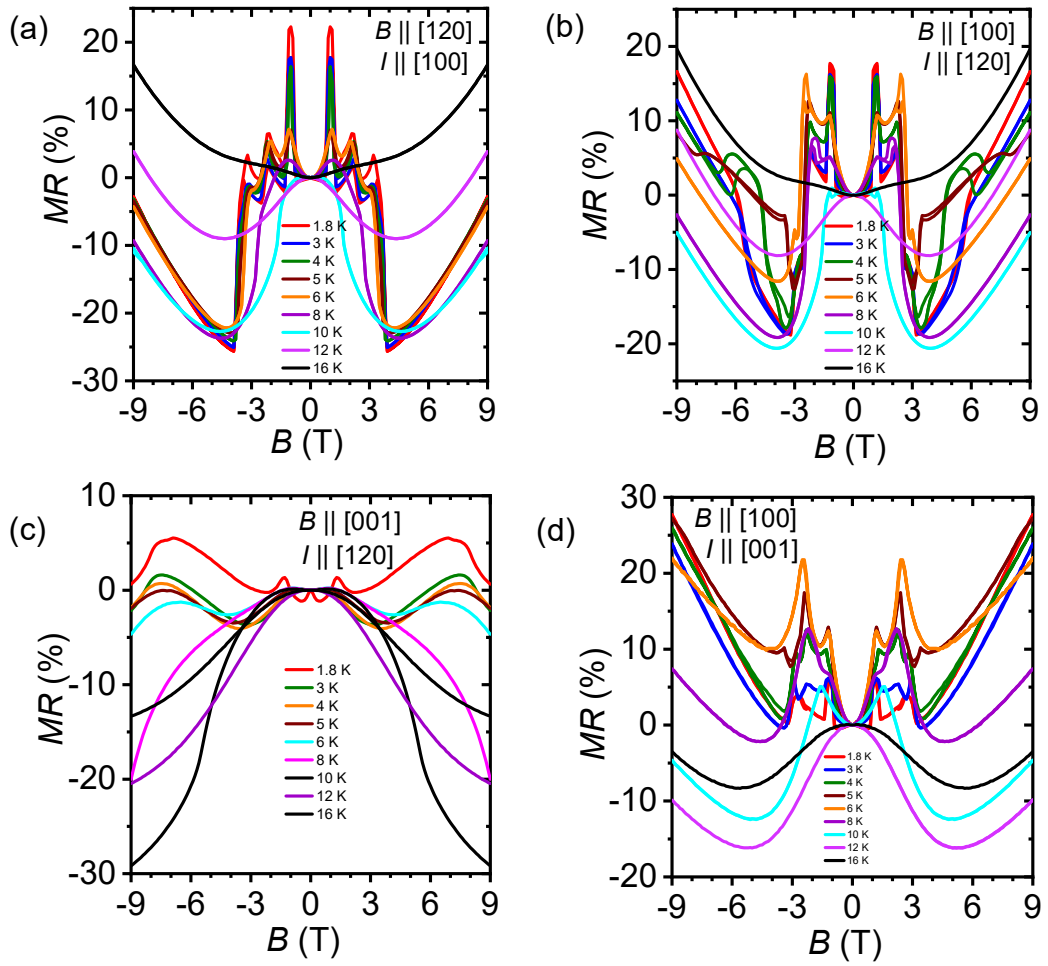

FIG. S6 : Magnetoresistance. Magnetoresistance (MR) as a function of magnetic field for (a) B|||[120] and I|||[100] and (b) B|||[100] and I|||[120] (c) B|||[001] and I|||[120], and (d) B|||[100] and I|||[001], respectively.

S4. STRUCTURAL CHARACTERIZATION

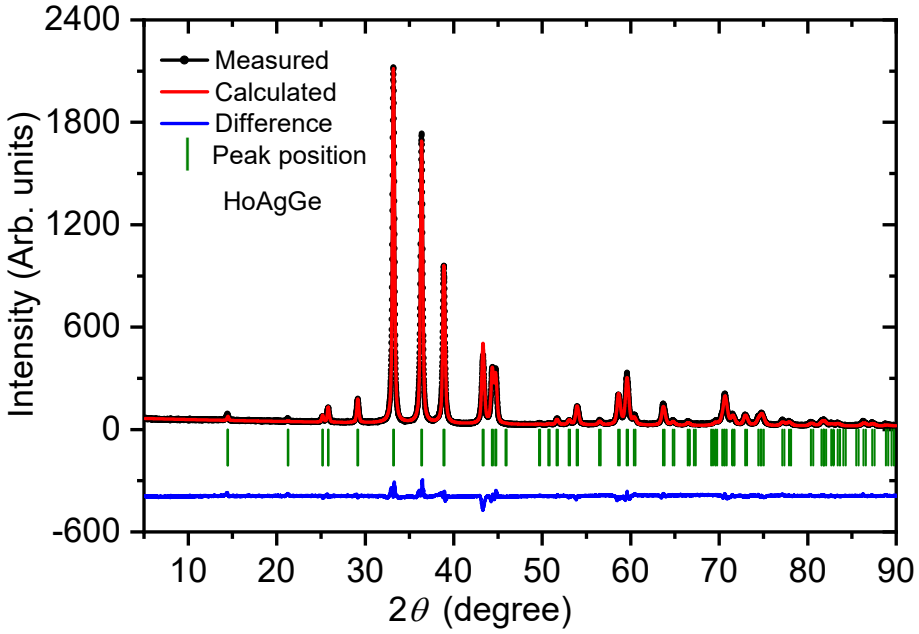

FIG. S7 : X-ray diffraction. Rietveld refinement of the X-ray powder pattern of HoAgGe measured at room temperature.

Space group	$P\bar{6}2m$ (No. 189)
Unit cell parameters	a = 7.0761(7) Å
	c = 4.1788(2) Å
R_{WP}	11.7 %
R_B	5.499 %
R_F	6.778 %

TABLE S2 : Selected data from Rietveld refinement of powder X-ray diffraction collected on ground crystals of HoAgGe. Atomic coordinates are 0.58481, 0, 0 for Ho; 0.24866, 0, $\frac{1}{2}$ for Ag; $\frac{1}{3}$, $\frac{2}{3}$, $\frac{1}{2}$ for Ge(1); and 0, 0, 0 for Ge(2).

S5. REFERENCES

[1] T. Ozaki, Physical Review B **67**, 155108 (2003).
[2] The code OPENMX pseudoatomic basis functions, and pseudopotentials are available under terms of the GNU-GPL on a web site, http://www.openmx-square.org/.
[3] V. Antropov, M. Katsnelson, and A. Liechtenstein, Physica B: Condensed Matter **237–238**, 336 (1997).
[4] M. I. Katsnelson and A. I. Lichtenstein, Physical Review B **61**, 8906 (2000).
[5] A. Terasawa, M. Matsumoto, T. Ozaki, and Y. Gohda, Journal of the Physical Society of Japan **88**, 114706 (2019).
[6] M. J. Han, T. Ozaki, and J. Yu, Physical Review B **70**, 184421 (2004).
[7] K. Zhao, Y. Tokiwa, H. Chen, and P. Gegenwart, Nature Physics **20**, 442 (2024).
[8] K. Zhao, H. Deng, H. Chen, K. A. Ross, V. Petříček, G. Günther, M. Russina, V. Hutanu, and P. Gegenwart, Science **367**, 1218 (2020).
[9] Y. Lee, R. Skomski, X. Wang, P. P. Orth, Y. Ren, B. Kang, A. K. Pathak, A. Kutepov, B. N. Harmon, R. J. McQueeney, I. I. Mazin, and L. Ke, Physical Review B **108**, 045132 (2023).